Atmos. Meas. Tech., 15, 6807–6817, 2022
https://doi.org/10.5194/amt-15-6807-2022

Atmospheric Measurement Techniques
Open Access
EGU

New method to determine black carbon mass size distribution

Weilun Zhao[1], Gang Zhao[2], Ying Li[3,4], Song Guo[2], Nan Ma[5], Lizi Tang[2], Zirui Zhang[2], and Chunsheng Zhao[1]

[1]Department of Atmospheric and Oceanic Sciences, School of Physics, Peking University, Beijing 100871, China
[2]State Key Joint Laboratory of Environmental Simulation and Pollution Control, College of Environmental Sciences and Engineering, Peking University, Beijing 100871, China
[3]Department of Ocean Science and Engineering, Southern University of Science and Technology, Shenzhen 518055, China
[4]Southern Marine Science and Engineering Guangdong Laboratory, Guangzhou 511458, China
[5]Institute for Environmental and Climate Research, Jinan University, Guangzhou 511443, China

Correspondence: Chunsheng Zhao (zcs@pku.edu.cn)

Received: 25 April 2022 – Discussion started: 20 May 2022
Revised: 10 November 2022 – Accepted: 10 November 2022 – Published: 23 November 2022

Abstract. Black carbon (BC) is an important atmospheric component with strong light absorption. Many attempts have been made to measure BC mass size distribution (BCMSD) for its significant impact on climate and public health. Larger-coverage BCMSD, ranging from upper submicron particles sizes to larger than 1 µm, contributes to a substantial proportion of total BC mass and absorption. However, the current time resolution of larger-coverage BCMSD measurement was limited to 1 d, which was insufficient to characterize variation of larger-coverage BCMSD. In this study, a new method to determine equivalent BCMSD (eBCMSD) was proposed from size-resolved absorption coefficient measured by an aerodynamic aerosol classifier in tandem with an aethalometer. The proposed method could measure larger-coverage eBCMSD with a time resolution as high as 1 h and was validated by comparing the measurement results with refractory BCMSD (rBCMSD) measured by a differential mobility analyzer in tandem with a single-particle soot photometer (DMA–SP2) for particle sizes larger than 300 nm during a field measurement in the Yangtze River Delta. Bulk refractory BC mass concentration ($m_{\mathrm{rBC,bulk}}$) by DMA–SP2 was underestimated by 33 % compared to bulk equivalent BC mass concentration ($m_{\mathrm{eBC,bulk}}$) by this method because of the limited size range of measurement for DMA–SP2. Uncertainty analysis of this method was performed with respect to mass absorption cross-section (MAC), transfer function inversion, number fraction of BC-containing particle and instrumental noise. The results indicated that MAC was the main uncertainty source, leading to $m_{\mathrm{eBC,bulk}}$ values that varied from −20 % to 28 %. With the advantage of a wide size coverage up to 1.5 µm, high time resolution, easy operation and low cost, this method is expected to have wide applications in field measurement for better estimating the radiative properties and climate effects of BC.

1 Introduction

Atmospheric black carbon (BC) is emitted through incomplete combustion of carbon-based fuels (Bond, 2001), such as biomass burning and fossil fuel combustion (Bond et al., 2004). BC warms the atmosphere and is considered the third most important light absorber in the climate system after CO_2 and CH_4 (Bond et al., 2013). BC can induce respiratory and cardiovascular disease through inhalation (Highwood and Kinnersley, 2006). Plenty of studies have been devoted to BC for its significant impact on the climate and on public health.

Bulk BC mass concentration ($m_{\mathrm{BC,bulk}}$) is one of the essential parameters for modeling because radiative transfer models calculate BC absorption from $m_{\mathrm{BC,bulk}}$ (Bond et al., 2013). A great deal of research has been dedicated to $m_{\mathrm{BC,bulk}}$ measurement for both model assimilation and environmental monitoring (Castagna et al., 2019; Helin et al., 2018; Ran et al., 2016). A recent study indicated that the radiative effect of BC was extremely sensitive to its particle size (Matsui et al., 2018). Zhao et al. (2019) further revealed that the variation of BC mass size distribution (BCMSD), namely size-resolved BC mass concentration ($m_{\mathrm{BC,size\text{-}resolved}}$), led to substantial changes in the ra-

diative effect of BC based on field measurement, highlighting the importance of BCMSD for modeling the radiative effect of BC rather than simply $m_{\mathrm{BC,bulk}}$. The size of BC affects the deposition rate of BC to the lungs (Highwood and Kinnersley, 2006), indicating that BCMSD is closely related to health. In ambient environments, BCMSD is influenced by emission sources. For instance, BCMSD of fossil fuel combustion differs obviously from that of biomass burning (Schwarz et al., 2008), implying that BCMSD is one of the characteristics of emission sources. The temporal variation of BCMSD can reflect the atmospheric aging of BC, during which BC undergoes remarkable change in size, accompanied by dramatic variation of BC optical properties (Zhang et al., 2008). Therefore, reliable measurement and understanding of BCMSD are highly necessary for estimating the impact of BC on both the earth energy budget and on public health (Moosmuller et al., 2009).

Quite a few efforts were made to measure BCMSD. The single-particle soot photometer (SP2) was developed using laser-induced incandescence (Schwarz et al., 2006) and measured refractory BCMSD (rBCMSD; Petzold et al., 2013) on a single-particle level. The soot particle aerosol mass spectrometer (SP-AMS) combined laser-induced incandescence and mass spectroscopy, which could determine not only rBCMSD, but also the chemical composition of BC-containing particles (Onasch et al., 2012). The SP2 and SP-AMS techniques were characterized by high time resolution and high accuracy but also high cost and complicated maintenance and therefore, as a result, not widely applied for routine measurement. A more convenient solution was required for wider and better characterization of BCMSD in different regions and emission sources. Elemental carbon mass size distribution (ECMSD; Petzold et al., 2013) could be sampled by a multi-stage cascade impactor (Viidanoja et al., 2002) combined with off-line analysis, such as a thermo-optical organic carbon–elemental carbon method (Chow et al., 2001). ECMSD sampled by a multi-stage cascade impactor had wide size coverage but low time resolution, usually from 24 h (Soto-García et al., 2011) to 48 h (Guo, 2015), which was too low to resolve aging of BC. A differential mobility analyzer (DMA) in tandem with a filter-based instrument (Hansen et al., 1984), for instance, a micro-aethalometer (MA) (Ning et al., 2013) or a particle soot absorption photometer (PSAP) (Tunved et al., 2021), was used to determine equivalent BCMSD (eBCMSD; Petzold et al., 2013) with a higher time resolution up to 2 h (W. Zhao et al., 2021). However, the multiple-charge correction and low flow rate of DMA imposed restrictions on the accuracy of the measured eBCMSD. The measured size range of DMA was limited to less than about 700 nm, resulting in incomplete measured eBCMSD. Current measurement of larger-coverage BCMSD, ranging from upper submicron particle sizes to larger than 1 µm, was limited in time resolution. Characteristics of larger-coverage BCMSD during atmospheric aging were still unclear. Wang et al. (2022) showed that BC larger than 1 µm could contribute to as large as 50 % of $m_{\mathrm{BC,bulk}}$, highlighting the importance of larger-coverage BCMSD. Therefore, it was imperative to measure larger-coverage BCMSD with a higher time resolution.

In this study, a new method to determine eBCMSD was proposed using a size-resolved absorption coefficient ($\sigma_{\mathrm{ab,size\text{-}resolved}}$) measured by an aerodynamic aerosol classifier (AAC; Cambustion, UK, Tavakoli and Olfert, 2013) in tandem with an aethalometer (model AE33, Magee, USA, Drinovec et al., 2015), combined with size-resolved number concentration ($N_{\mathrm{size\text{-}resolved}}$), simultaneously measured by a scanning mobility particle sizer (SMPS; TSI, USA) and an aerodynamic particle sizer (APS; TSI, USA). The proposed method for determining eBCMSD overcame the disadvantages and had the advantages of the above-mentioned methods, characterized by high cost-effectiveness, easy and convenient maintenance, a high time resolution to 1 h and a wide size range to up to 1.5 µm. The proposed method was validated in a field measurement in the Yangtze River Delta, and the uncertainty study was carried out based on the measured data.

2 Methods

2.1 Instrumental setup

Figure 1 illustrated the instrumental setup developed in this study, which could be split into two parts, namely the measurement setup and the validation setup. Ambient aerosol particles were drawn through a PM_{10} inlet ($16.67\,\mathrm{L\,min^{-1}}$) and were dried to a relative humidity of less than 30 % by a silica gel diffusion dryer beforehand. An advanced flow splitter was used to split aerosol-laden flow into different instruments for isokinetic sampling. For the measurement setup, AAC in tandem with AE33 (AAC–AE33) measured $\sigma_{\mathrm{ab,size\text{-}resolved}}$ at a flow rate of $3\,\mathrm{L\,min^{-1}}$. Since eBCMSD of larger size coverage was the main focus of this study, AAC was set to scan 12 particle sizes (D_{p}) logarithmically equally spaced from 200 to 1500 nm (200, 240, 288, 346, 416, 499, 600, 720, 865, 1039, 1248 and 1500 nm), and a smaller size was not scanned. Each size was scanned for 5 min, and 1 h was required for a complete cycle. It should be noted that D_{p} was the aerodynamic size in this study. Mobility size related to DMA was converted to aerodynamic size, assuming an effective density of $1.3\,\mathrm{g\,cm^{-3}}$ (Zhao et al., 2019; DeCarlo et al., 2004). AE33 measured absorption coefficient (σ_{ab}) at seven wavelengths from 370 to 950 nm (Drinovec et al., 2015), at which 880 nm was adopted in this study because BC dominated particle absorption at 880 nm (Ramachandran and Rajesh, 2007). SMPS and APS measured $N_{\mathrm{size\text{-}resolved}}$ for D_{p} less than and greater than about 800 nm at a flow rate of 0.3 and $5\,\mathrm{L\,min^{-1}}$, respectively.

For validation system, the tandem array of a neutralizer, DMA and SP2 (DMA–SP2) measured rBCMSD

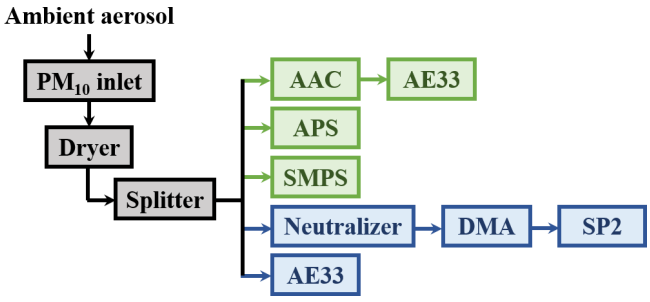

Figure 1. Schematic diagram of the measurement (green) and the validation (blue) setup.

($\mathrm{rBCMSD_{DMA-SP2}}$) at a flow rate of $0.12\,\mathrm{L\,min^{-1}}$ for the purpose of comparison with eBCMSD determined by the proposed method ($\mathrm{eBCMSD_{AAC-AE33}}$). Another AE33 measured the bulk absorption coefficient ($\sigma_{\mathrm{ab,bulk}}$) simultaneously at a flow rate of $2\,\mathrm{L\,min^{-1}}$ for a closure study with $\sigma_{\mathrm{ab,size\text{-}resolved}}$.

2.1.1 Aethalometer model AE33

The principle of obtaining σ_{ab} was well developed for an aethalometer (Hansen et al., 1984) and is described here in brief. Ambient aerosol particles were drawn into an aethalometer at a flow rate F and collected on an area S of a filter. A light source illuminated the filter. The transmitted light signal was denoted as I (I_0) for the light which passed through the particle-laden (particle-free) part of the filter. Light attenuation was defined as

$$\mathrm{ATN} = -100 \cdot \ln\left(\frac{I}{I_0}\right). \tag{1}$$

ATN increased with decreasing I as aerosol particles were loaded on the filter continuously. Therefore, ATN reflected aerosol loading on the filter. If ATN increased $\Delta\mathrm{ATN}$ during time interval Δt, then the attenuation coefficient was defined as

$$\sigma_{\mathrm{ATN}} = \frac{S}{100 \cdot F} \cdot \frac{\Delta\mathrm{ATN}}{\Delta t}. \tag{2}$$

The light attenuation was caused not only by particle absorption, but also scattering by the particle and filter matrix. A scattering parameter C_{f} was introduced to extract σ_{ab} from σ_{ATN}:

$$\sigma_{\mathrm{ab}} = \frac{\sigma_{\mathrm{ATN}}}{C_{\mathrm{f}}}, \tag{3}$$

where C_{f} was set as 2.9 (Zhao et al., 2020b) in this study. Nonlinearity, termed the loading effect, became more and more significant with increasing aerosol loading; namely, for the same increase in aerosol loading, the corresponding increase in ATN was smaller for heavier aerosol loading. The "dual-spot" technique (Drinovec et al., 2015) was proposed to correct for the loading effect for AE33 and was used in this study. The σ_{ab} measured by AE33 at a given particle size selected by AAC was termed binned σ_{ab} ($\sigma_{\mathrm{ab,binned}}$) in this study to differentiate from $\sigma_{\mathrm{ab,bulk}}$.

2.1.2 Aerodynamic aerosol classifier

The principle of the AAC was illustrated detailedly by Tavakoli and Olfert (2013) and was introduced here concisely. The setup of the AAC could be simplified to two coaxial cylinders, where the inner radius, outer radius and length were denoted as r_{i}, r_{o} and L. Polydisperse particles flowed into the space between the inner cylinder and outer cylinder from one end of the inner cylinder at a flow rate of Q_{sample}. Meanwhile, particle-free sheath flow streamed in the space between the inner cylinder and outer cylinder in the direction of the axis of the coaxial cylinders at a flow rate of Q_{sheath}. The sheath flow carried the particles along the coaxial cylinders. At the same time, the two coaxial cylinders rotated with respect to their axis at a rotational speed of ω. Therefore, the particles migrated outwards across the sheath flow by the centrifugal force acting on them. Relaxation time (τ) was defined as

$$\tau = \frac{C_{\mathrm{c}}\left(D_{\mathrm{p}}\right)\rho_0 D_{\mathrm{p}}^2}{18\,\mu}, \tag{4}$$

where $C_{\mathrm{c}}(D_{\mathrm{p}})$ was the Cunningham slip correction factor as a function of D_{p} (Kim et al., 2005), $\rho_0 = 1\,\mathrm{g\,cm^{-3}}$ was the reference density and μ was the gas viscosity. It could be seen that τ was directly related to D_{p}. Dynamic analysis proved that only particles with certain relaxation time τ, and hence certain D_{p}, could migrate to another end of the outer cylinder and emerge as monodisperse flow. τ was related to parameters of the AAC by

$$\tau = \frac{2Q_{\mathrm{sheath}}}{\pi\omega^2(r_{\mathrm{i}}+r_{\mathrm{o}})^2 L}. \tag{5}$$

Therefore, by changing ω and Q_{sheath}, monodisperse particles of desired D_{p} could be selected by the AAC. Unlike the DMA, particles did not need to be charged before entering the AAC. Consequently, the transmission efficiency (λ_Ω) of the AAC was about 4 times higher than that of the DMA, and multi-charge correction was not required for AE33 (Johnson et al., 2018).

2.1.3 A differential mobility analyzer in tandem with a single-particle soot photometer

Ambient particles were first drawn into a DMA, which could select monodispersed particles with D_{p} from the polydispersed ambient particles. Then the monodispersed particles flew into the SP2, which measured refractory black carbon (rBC) mass of BC-containing particles on a single-particle level. $\mathrm{rBCMSD_{DMA-SP2}}$ was measured by changing D_{p} selected by DMA and measuring rBC mass at different D_{p}s. The SP2 alone could also determine rBCMSD

($rBCMSD_{SP2}$). Considering that D_p of $rBCMSD_{SP2}$ was calculated from Mie theory with assumed inputs (Taylor et al., 2015), and D_p of $rBCMSD_{DMA-SP2}$ was directly measured by DMA, $rBCMSD_{DMA-SP2}$ was used in this study.

Details of DMA–SP2 were described by G. Zhao et al. (2021) and introduced here concisely. The incandescence high-gain channel and the incandescence low-gain channel of SP2 were calibrated by Aquadag soot particles with an effective density of $1.8\,g\,cm^{-3}$ before measurement. The DMA was set to scan D_p from 15 to 780 nm with 56 bins, and one scan cycle required 5 min. Therefore, time resolution and size range of the measured $rBCMSD_{DMA-SP2}$ were 5 min and from 15 to 780 nm. Considering that the time resolution of $eBCMSD_{AAC-AE33}$ was 1 h, the measured $rBCMSD_{DMA-SP2}$ was time-averaged to a time resolution of 1 h for comparison. Given that the size range of $eBCMSD_{AAC-AE33}$ was from 200 to 1500 nm, the size range of the measured $rBCMSD_{DMA-SP2}$ was interpolated to that of $eBCMSD_{AAC-AE33}$ for comparison. Consequently, the size range of $rBCMSD_{DMA-SP2}$ used in this study was from 200 to 720 nm, corresponding to the first and eighth D_p of $eBCMSD_{AAC-AE33}$, respectively. According to Zhao et al. (2020a), DMA–SP2 could not detect particle less than about 200 nm, consistent with the minimum D_p in this study.

The number distribution of BC-containing particles measured by DMA–SP2 could be considered a bivariate function $\frac{\partial^2 N_{BC}}{\partial \log D_p \partial \log D_c}$, where N_{BC} was the number concentration of BC-containing particles, and D_c was the core diameter assuming that BC-containing particles had a core–shell geometry. The asphericity of BC was not considered in this study. D_c was logarithmically equally distributed from 78 to 560 nm with 29 bins. At each D_c bin, the number distribution of BC-containing particle could be considered a univariate function $\frac{dN_{BC}}{d\log D_p}$. The multiple charging correction of 1-dimensional size distribution was developed by Knutson and Whitby (1975), which was adopted to correct $\frac{dN_{BC}}{d\log D_p}$. By correcting $\frac{dN_{BC}}{d\log D_p}$ at each D_c bin, multiple charging correction of $\frac{\partial^2 N_{BC}}{\partial \log D_p \partial \log D_c}$ was achieved.

2.2 Field measurement

The proposed method was applied to a field measurement in Changzhou, Jiangsu Province, China (119°36′ E, 31°43′ N), located in the Yangtze River Delta, from 17 May to 3 June 2021. Changzhou is between two megacities, about 187 km to the northwest of Shanghai and about 82 km to the southeast of Nanjing, as shown in Fig. S1a in the Supplement. The area between Shanghai and Nanjing has undergone serious environmental pollution in the past few decades with the development of industrialization and urbanization. As shown in Fig. S1b, the pollution condition of Changzhou was overall representative of the regional background pollution in the Yangtze River Delta.

2.3 Size-resolved calculations

2.3.1 Size-resolved absorption coefficient

Tavakoli and Olfert (2013) formulated the ideal theoretical model for AAC transfer function inversion, which was adopted by this study to derive $\sigma_{ab,size\text{-}resolved}$ from $\sigma_{ab,binned}$ and presented here in short. The $\sigma_{ab,size\text{-}resolved}$ was given by

$$\sigma_{ab,size\text{-}resolved} = \frac{d\sigma_{ab}}{d\log D_p} = \frac{\ln(10)}{\frac{d\log D_p}{d\log \tau}\cdot \beta^*}\cdot \sigma_{ab,binned}, \quad (6)$$

where β^* was related to the ratio of Q_{sheath} to Q_{sample}, $R_t = Q_{sheath}/Q_{sample} = 1/\beta$, through

$$\beta^* = \left(1+\frac{1}{\beta}\right)\ln(1+\beta) - \left(1-\frac{1}{\beta}\right)\ln(1-\beta). \quad (7)$$

Johnson et al. (2018) corrected the ideal inversion in Eq. (6) to take particle loss and spectral broadening into account by replacing β^* with a nonideal β^*_{NI}:

$$\beta^*_{NI} = \lambda_\Omega \mu_\Omega \left[\ln\left(\frac{1+\beta/\mu_\Omega}{1-\beta/\mu_\Omega}\right) + \frac{\mu_\Omega}{\beta}\ln\left(1-\left(\frac{\beta}{\mu_\Omega}\right)^2\right)\right], \quad (8)$$

where μ_Ω was the spectral broadening factor. Both λ_Ω and μ_Ω were dependent on D_p as well as flow, and this is discussed in detail in Sect. 4.2.

2.3.2 eBC mass size distribution measured by the aerodynamic aerosol classifier in tandem with the aethalometer model AE33

$\sigma_{ab,size\text{-}resolved}$ could be converted to $eBCMSD_{AAC-AE33}$ through mass absorption cross-section (MAC) (Bond and Bergstrom, 2006), which was determined based on method proposed by W. Zhao et al. (2021). Briefly, a 2-dimensional lookup table of MAC with respect to D_p and D_c was simulated ($MAC(D_p, D_c)$) by Mie theory, assuming a core–shell geometry. At a given size bin centered at D_p, the corresponding σ_{ab} and number concentration (N) at the size bin, denoted as $\sigma_{ab}(D_p)$ and $N(D_p)$, could be derived by $\sigma_{ab,size\text{-}resolved}$ and $N_{size\text{-}resolved}$:

$$\sigma_{ab}\left(D_p\right) = \sigma_{ab,size\text{-}resolved}\left(D_p\right)\cdot \Delta\log D_p, \quad (9)$$

$$N\left(D_p\right) = N_{size\text{-}resolved}\left(D_p\right)\cdot \Delta\log D_p, \quad (10)$$

where $\Delta\log D_p$ was the logarithmic width of the size bin. The number concentration of BC-containing particles at the size bin $N_{BC}(D_p)$ was determined by

$$N_{BC}\left(D_p\right) = N\left(D_p\right)\cdot f_{BC}, \quad (11)$$

where f_{BC} was the number fraction of BC-containing particles, which was assumed as a fixed value in this study, and the uncertainty of the fixed-f_{BC} assumption is discussed in

Sect. 4.3. An optimal D_c was found so that calculated σ_{ab} at the size bin, denoted as $\sigma_{ab,calc}(D_p, D_c)$, matched $\sigma_{ab}(D_p)$:

$$\sigma_{ab,calc}\left(D_p, D_c\right) = \rho_{BC}\frac{\pi}{6}D_c^3 \cdot \mathrm{MAC}\left(D_p, D_c\right) \cdot N_{BC}\left(D_p\right) = \sigma_{ab}\left(D_p\right), \quad (12)$$

where ρ_{BC} was the density of BC and set as $1.8\,\mathrm{g\,cm^{-3}}$ (Bond and Bergstrom, 2006), consistent with the ρ_{BC} assumption when deriving $\mathrm{rBCMSD_{DMA-SP2}}$. Equivalent BC mass concentration (m_{eBC}) at the size bin, denoted as $m_{eBC}(D_p)$, could be determined by

$$m_{eBC}\left(D_p\right) = \frac{\sigma_{ab}\left(D_p\right)}{\mathrm{MAC}\left(D_p, D_c\right)}. \quad (13)$$

Then the $\mathrm{eBCMSD_{AAC-AE33}}$ at D_p, denoted by $\mathrm{eBCMSD_{AAC-AE33}}(D_p)$, could be determined by

$$\mathrm{eBCMSD}\left(D_p\right) = \frac{m_{eBC}\left(D_p\right)}{\Delta \log D_p}. \quad (14)$$

3 Results and discussion

Figure 2 presents the time series of the measurement results. There were four pollution episodes during the measurement period: from about 12:00 on 17 May to about 00:00 on 20 May, from about 00:00 on 21 May to about 12:00 on 22 May, from about 00:00 on 24 May to about 12:00 on 26 May and from about 12:00 on 28 May to about 12:00 on 31 May, as shown in Fig. 2a. Both $\mathrm{eBCMSD_{AAC-AE33}}$ (Fig. 2b) and $\mathrm{rBCMSD_{DMA-SP2}}$ (Fig. 2c) recorded the four pollution episodes simultaneously, with higher BCMSD values than clean episodes. $\mathrm{eBCMSD_{AAC-AE33}}$ and $\mathrm{rBCMSD_{DMA-SP2}}$ were both integrated from 200 to 720 nm, which was the D_p range of measurement for DMA–SP2, and the results were denoted as $m_{eBC,bulk,AAC-AE33,200-720}$ and $m_{rBC,bulk,DMA-SP2,200-720}$, respectively. As shown in Fig. 2a, $m_{eBC,bulk,AAC-AE33,200-720}$ compared well with $\mathrm{m_{rBC,bulk,DMA-SP2,200-720}}$ with a determination coefficient (R^2), slope (b_1) and intercept (b_0) of 0.8 (accurate to one decimal place), 1.0 and $0.1\,\mu\mathrm{g\,m^{-3}}$ (Fig. S2a). R^2 of 0.8 and b_1 of 1.0 indicated that the proposed method was capable of capturing the variation of $m_{BC,bulk}$. The mean $m_{eBC,bulk,AAC-AE33,200-720}$ and $m_{rBC,bulk,DMA-SP2,200-720}$ were 0.7 ± 0.4 and $0.6 \pm 0.3\,\mu\mathrm{g\,m^{-3}}$, indicating $m_{eBC,bulk,AAC-AE33,200-720}$ was overall $0.1\,\mu\mathrm{g\,m^{-3}}$ higher than $m_{rBC,bulk,DMA-SP2,200-720}$, consistent with b_0 of $0.1\,\mu\mathrm{g\,m^{-3}}$. The reason for overall discrepancy of $0.1\,\mu\mathrm{g\,m^{-3}}$ in $m_{BC,bulk,200-720}$ might be that DMA–SP2 could not detect rBC with D_c less than about 100 nm (Zhao et al., 2020a), resulting in an underestimated $m_{rBC,bulk,DMA-SP2,200-720}$. $\mathrm{eBCMSD_{AAC-AE33}}$ was also integrated from 720 to 1500 nm, which was the D_p range that DMA–SP2 did not measure, and the result was denoted as $m_{eBC,bulk,AAC-AE33,720-1500}$. $m_{eBC,bulk,AAC-AE33,720-1500}$ was correlated to $m_{rBC,bulk,DMA-SP2,200-720}$ to study whether BCMSD ranging from 720 to 1500 nm was connected to that ranging from 200 to 720 nm, as shown in Fig. S2b. R^2 decreased to 0.2 between $m_{eBC,bulk,AAC-AE33,720-1500}$ and $m_{rBC,bulk,DMA-SP2,200-720}$, indicating these two size ranges were not well related, and both of them needed to be measured independently. Observation by transmission electron microscopy showed that these larger BC-containing particles could be coated with massive materials from secondary processes or super-aggregated BC with a fractal BC structure (Wang et al., 2022). The mean $m_{eBC,bulk,AAC-AE33,720-1500}$ was $0.2 \pm 0.2\,\mu\mathrm{g\,m^{-3}}$, indicating that the DMA–SP2 overall underestimated $m_{BC,bulk}$ for $\sim 0.2\,\mu\mathrm{g\,m^{-3}}$ ($\sim 33\,\%$) in this field measurement considering that the DMA–SP2 did not measure BCMSD larger than 720 nm. Therefore, it is highly necessary to measure BCMSD with a wider D_p range for better estimation of $m_{BC,bulk}$ and deeper understanding of BC evolution in the atmosphere.

Figure 3 exhibited the mean $\mathrm{eBCMSD_{AAC-AE33}}$ ($\overline{\mathrm{eBCMSD}}_{\mathrm{AAC-AE33}}$) and mean $\mathrm{rBCMSD_{DMA-SP2}}$ ($\overline{\mathrm{rBCMSD}}_{\mathrm{DMA-SP2}}$) during the field measurement. It could be seen that when D_p was less than about 300 nm, $\overline{\mathrm{eBCMSD}}_{\mathrm{AAC-AE33}}$ was higher than $\overline{\mathrm{rBCMSD}}_{\mathrm{DMA-SP2}}$. The higher $\overline{\mathrm{eBCMSD}}_{\mathrm{AAC-AE33}}$ may be due to particle diffusion at small D_p, which was not well corrected by Eq. (7) and underestimated MAC. When D_p was greater than 300 nm and less than 720 nm, $\overline{\mathrm{eBCMSD}}_{\mathrm{AAC-AE33}}$ was overall consistent with $\overline{\mathrm{rBCMSD}}_{\mathrm{DMA-SP2}}$. When D_p was larger than 720 nm, where DMA–SP2 did not measure, $\overline{\mathrm{eBCMSD}}_{\mathrm{AAC-AE33}}$ decreased with increasing D_p when D_p was less than about 870 nm and increased with increasing D_p when D_p was larger than 870 nm. In the study by Yu et al. (2010), three modes of BCMSD were identified: the mode peaked at about 400, 1000 and 5000 nm, which were termed as the condensation mode, droplet mode and coarse mode, respectively. Following the nomenclature proposed by Yu et al. (2010), the increasing (decreasing) $\overline{\mathrm{eBCMSD}}_{\mathrm{AAC-AE33}}$ with increasing D_p for D_p larger (less) than 870 nm signified the lower (upper) end of the droplet mode (condensation mode). However, $\overline{\mathrm{rBCMSD}}_{\mathrm{DMA-SP2}}$ only identified the condensation mode, which clearly highlighted the necessity to measure BCMSD of a wider D_p range for better characterization of BCMSD. Both the proposed method and the DMA–SP2 showed that the temporal variation of BCMSD, expressed as standard deviation (SD) of BCMSD in Fig. 3, was as large as $\overline{\mathrm{BCMSD}}$, reflecting complex mechanisms in the variability of BCMSD.

4 Uncertainty analysis

Uncertainty analysis was performed with respect to the MAC lookup table, transfer function inversion from $\sigma_{ab,binned}$ to

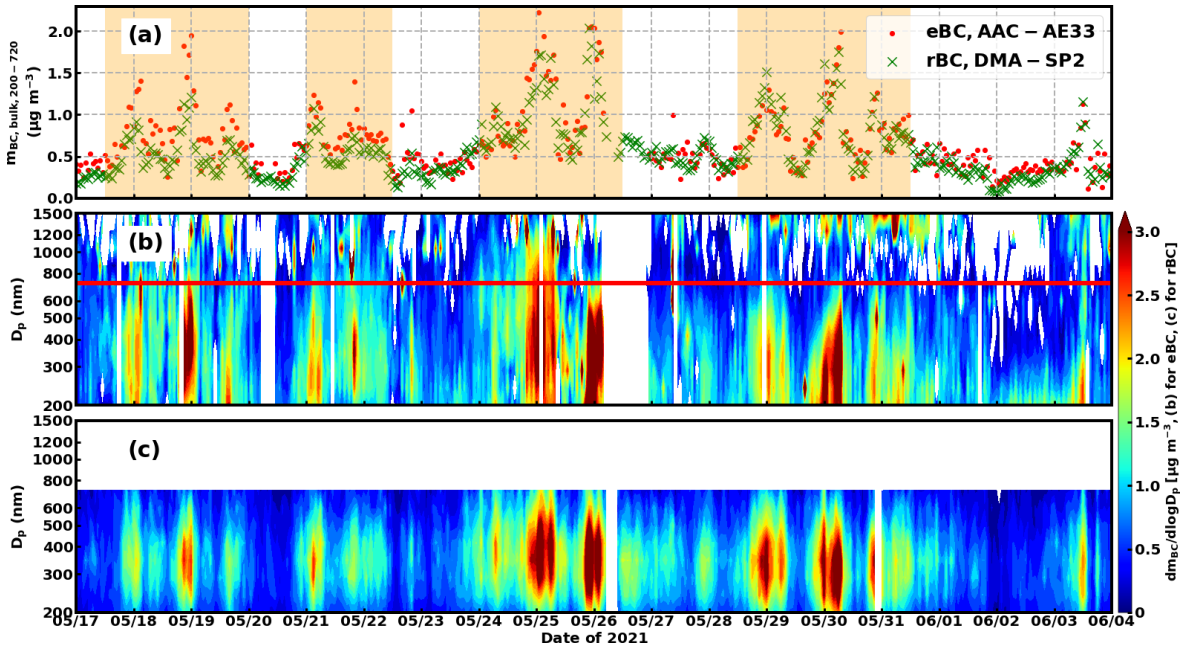

Figure 2. Time series of **(a)** $m_{BC,bulk}$ from BCMSD integrated from 200 to 720 nm ($m_{BC,bulk,200-720}$) determined by the proposed method (red dot, denoted as "eBC, AAC–AE33") and the DMA–SP2 (green cross, denoted as "rBC, DMA–SP2") and BCMSD determined by **(b)** the proposed method (eBC) and **(c)** the DMA–SP2 (rBC). The red line in panel **(b)** marks a particle size of 720 nm. The pollution episodes are shaded with orange in panel **(a)**.

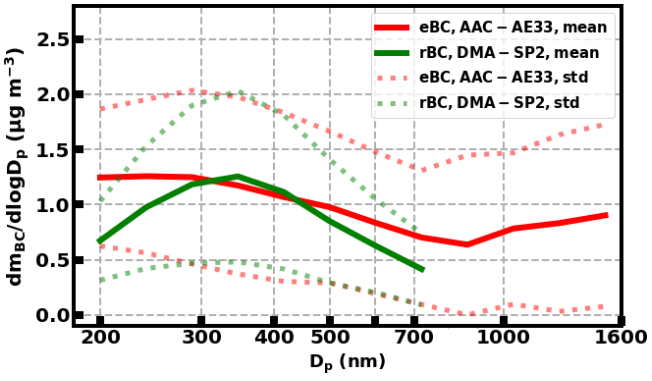

Figure 3. Mean and SD of $eBCMSD_{AAC-AE33}$ (green) and $rBCMSD_{DMA-SP2}$ (red) during the measurement period. Mean BCMSD was denoted by the solid line. SD of BCMSD was denoted by the dotted line.

$\sigma_{ab,size\text{-}resolved}$, f_{BC} and instrumental noise, respectively. The resulting uncertainty to $eBCMSD_{AAC-AE33}$ is illustrated in Fig. 4 and to $m_{eBC,bulk,AAC-AE33,200-720}$ is shown in Table 1. It can be seen from Fig. 4 that the boundary between the condensation mode and the droplet mode was distinct, no matter how the uncertainty sources disturbed $eBCMSD_{AAC-AE33}$.

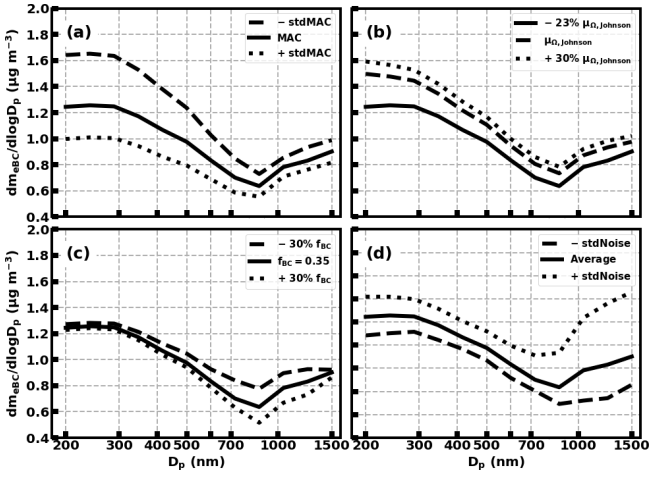

Figure 4. Uncertainty in $eBCMSD_{AAC-AE33}$ arising from **(a)** MAC lookup table, **(b)** transfer function inversion, **(c)** f_{BC} and **(d)** instrumental noise. The solid lines in each panel were the same and were the mean $eBCMSD_{AAC-AE33}$ during the measurement period. The dotted lines and dashed lines in each panel were mean $eBCMSD_{AAC-AE33} \pm$ standard deviation (SD) calculated from **(a)** MAC + SD of MAC and MAC − SD of MAC, **(b)** $\mu_{\Omega,Johnson}$ and $1.3 \times \mu_{\Omega,Johnson}$, **(c)** f_{BC} of 35 % ×0.7 and 1.3, and **(d)** $eBCMSD_{AAC-AE33}$ + SD of instrumental noise and − SD of instrumental noise.

4.1 Uncertainty from mass absorption cross-section

According to W. Zhao et al. (2021), the variation in the refractive index (RI) dominated the uncertainty of the MAC lookup table. Therefore, the uncertainty from the MAC lookup table was analyzed with respect to RI. The real part of RI (*Re*[RI]) was reported to vary from 1.5 to 2.0 in general (Liu et al., 2018), and the imaginary part of RI (*Im*[RI]) ranged from 0.5 to 1.1 commonly (Bond and Bergstrom, 2006). Hence, *Re*[RI] (*Im*[RI]) was changed from 1.5 (0.5) to 2.0 (1.1) with step increase of 0.01, the resulting mean MAC ($\overline{\mathrm{MAC}}$) was the MAC lookup table used in this study (Fig. S3a) and the resulting SD divided by the $\overline{MAC}$ was considered the uncertainty of the MAC lookup table (Fig. S3b). As shown in Fig. S3b, when D_c was larger than about 400 nm, the uncertainty was less than 10 % and influenced by both D_p and D_c. However, when D_c was less than 400 nm, the uncertainty increased rapidly with decreasing D_c and was dominated by D_c. The uncertainty increased to larger than 23 % when D_c was less than about 100 nm. When D_p was less than about 300 nm, the uncertainty varied from 14 % to 24 % with a mean value of 22 %, indicating large uncertainty in $\mathrm{eBCMSD}_{\mathrm{AAC-AE33}}$ for D_p less than 300 nm.

The MAC lookup table was replaced with original $\overline{\mathrm{MAC}}$ minus its SD (−SDMAC) and plus its SD (+SDMAC). The resulting MAC lookup tables were taken into the method proposed by W. Zhao et al. (2021) and applied to the entire measurement period to study the influence of MAC variation on the $\mathrm{eBCMSD}_{\mathrm{AAC-AE33}}$. $\overline{\mathrm{eBCMSD}}_{\mathrm{AAC-AE33}}$ and mean $\mathrm{eBCMSD}_{\mathrm{AAC-AE33}}$ after ± SDMAC are shown in Fig. 4a. The uncertainty increased with decreasing D_p and reached a maximum when D_p was less than 300 nm, indicating the $\mathrm{eBCMSD}_{\mathrm{AAC-AE33}}$ for D_p less than 300 nm might potentially have non-negligible uncertainty. The uncertainty in $m_{\mathrm{eBC,bulk,AAC-AE33,200-720}}$ was from −20 % (+SDMAC) to +28 % (−SDMAC), which was the largest among the four uncertainty sources, as shown in Table 1.

4.2 Uncertainty from the transfer function inversion

As stated in Sect. 2.4.1, correction for particle loss and spectral broadening was required when $\sigma_{\mathrm{ab,binned}}$ was converted to $\sigma_{\mathrm{ab,size\text{-}resolved}}$. λ_Ω was defined to correct particle loss where $\lambda_\Omega = 0 (\lambda_\Omega = 1)$ stood for total (no) particle loss. The relationships between λ_Ω and D_p as well as Q_{sample}, as shown in Fig. S4a, were well developed (Karlsson and Martinsson, 2003) and consistent with experimental data of the AAC (Johnson et al., 2018). Q_{sample} used in this study was $3.0\,\mathrm{L\,min^{-1}}$. Q_{sample} was changed from −30 % ($2.1\,\mathrm{L\,min^{-1}}$) to +30 % ($3.9\,\mathrm{L\,min^{-1}}$), and the resulting λ_Ω was used to study the fluctuation of Q_{sample} on λ_Ω. As shown in Fig. S4a, the variation of λ_Ω was less than 0.5 %, which was negligible.

Spectral broadening was caused by small-size particle diffusion as well as disturbance of sheath flow due to complicated rotation fluid dynamics inside the AAC and described by μ_Ω, where $\mu_\Omega < 1$ ($\mu_\Omega = 1$) was for (no) broadening. Johnson et al. (2018) found that behavior of μ_Ω with respect to D_p ($\mu_\Omega(D_p)$) depended on both Q_{sheath} and Q_{sample} and parameterized $\mu_\Omega(D_p)$ (Fig. S4b) based on two case studies of Q_{sheath} and Q_{sample}, namely $3\,\mathrm{L\,min^{-1}}$ and $0.3\,\mathrm{L\,min^{-1}}$ and $15\,\mathrm{L\,min^{-1}}$ and $1.5\,\mathrm{L\,min^{-1}}$:

$$\mu_{\Omega,\mathrm{Johnson}}\left(D_p\right) = 0.318 \cdot D_p^{0.0946}. \quad (15)$$

Q_{sheath} and Q_{sample} were $7.5\,\mathrm{L\,min^{-1}}$ and $3\,\mathrm{L\,min^{-1}}$ in this study, which might have led to uncertainty if $\mu_{\Omega,\mathrm{Johnson}}(D_p)$ had been directly used in this study. $\mu_{\Omega,\mathrm{Johnson}}(D_p)$ was varied from −23 % to +30 % to study the impact of μ_Ω on $\mathrm{eBCMSD}_{\mathrm{AAC-AE33}}$. The resulting influence on the $\mathrm{eBCMSD}_{\mathrm{AAC-AE33}}$ is shown in Fig. 4b. The uncertainty of μ_Ω did not exhibit a significant size dependence. Lower μ_Ω led to lower $\mathrm{eBCMSD}_{\mathrm{AAC-AE33}}$, and vice versa. The difference in the $m_{\mathrm{eBC,bulk,AAC-AE33,200-720}}$ was from −1 % (−23 % of $\mu_{\Omega,\mathrm{Johnson}}$) to +21 % (+30 % of $\mu_{\Omega,\mathrm{Johnson}}$), implying systematic overestimation of $m_{\mathrm{eBC,bulk,AAC-AE33,200-720}}$. Therefore, $\mu_\Omega(D_p) = 77\,\% \ \mu_{\Omega,\mathrm{Johnson}}(D_p)$ was used in this study to offset the bias. The reason for the lower limit of μ_Ω set as −23 % rather than −30 % was that $\mathrm{eBCMSD}_{\mathrm{AAC-AE33}}$ was invalid mathematically when μ_Ω was less than −23 % under the setting of (Q_{sheath}, Q_{sample}) used in this study. It should be pointed out that AAC–AE33 could still determine valid eBCMSD under the condition of $\mu_\Omega(D_p) < 77\,\% \ \mu_{\Omega,\mathrm{Johnson}}(D_p)$ by increasing Q_{sheath}. Q_{sheath} was not changed in this study because desired $\mu_\Omega(D_p)$ parameterization was found at $\mu_\Omega(D_p) = 77\,\% \ \mu_{\Omega,\mathrm{Johnson}}(D_p)$.

$\sigma_{\mathrm{ab,size\text{-}resolved}}$ (Fig. S5b) was integrated, and the result, denoted as $\sigma_{\mathrm{ab,bulk,calc}}$, was compared to $\sigma_{\mathrm{ab,bulk}}$. As shown in Fig. S5a, $\sigma_{\mathrm{ab,bulk,calc}}$ was consistent with $\sigma_{\mathrm{ab,bulk}}$. R^2, b_1 and b_0 between $\sigma_{\mathrm{ab,bulk,calc}}$ and $\sigma_{\mathrm{ab,bulk}}$ were 0.9, 1.1 and $0.5\,\mathrm{M\,m^{-1}}$ (Fig. S6), respectively, which validated conversion from $\sigma_{\mathrm{ab,binned}}$ to $\sigma_{\mathrm{ab,size\text{-}resolved}}$.

4.3 Uncertainty from number fraction of BC-containing particle

BC-containing aerosol particles had complicated mixing states. Even for internally mixed particles with the same D_p, the internal BC cores might have different D_c, which could not be resolved by AAC–AE33. Field measurement (Liu et al., 2010) revealed that f_{BC} varied with time, D_c and D_p. This complexity was simplified to a parameterized fixed value of f_{BC} in this study. A fixed f_{BC} implied that only one D_c value corresponded to a given D_p and the size-resolved number concentration of BC-containing particle was determined by $N_{\mathrm{size\text{-}resolved}}$ times f_{BC}. W. Zhao et al. (2021) used a f_{BC} value of 0.17 based on SP2 measurement. However, SP2-derived f_{BC} could not represent

Table 1. The uncertainty in the $m_{\mathrm{eBC,bulk,AAC-AE33,200-720}}$ that resulted from the MAC lookup table, transfer function inversion, f_{BC} and instrumental noise.

Uncertainty source	MAC	Transfer function inversion	f_{BC}	Instrumental noise
Uncertainty	−20 % to +28 %	−1 % to +21 %	−3 % to +3 %	−2 % to −1 %

the bulk f_{BC} over the whole particle size spectrum due to the detection limit of SP2. And different regions might have different f_{BC}. In this study, f_{BC} was varied, and the resulting $m_{\mathrm{eBC,bulk,AAC-AE33,200-720}}$ was compared with $m_{\mathrm{rBC,bulk,DMA-SP2,200-720}}$. f_{BC} was set as 0.35 in this study because b_1 was 1.0 between $m_{\mathrm{eBC,bulk,AAC-AE33,200-720}}$ and $m_{\mathrm{rBC,bulk,DMA-SP2,200-720}}$ when f_{BC} was 0.35.

f_{BC} was varied from 0.25 (−30 % of 0.35) to 0.46 (+30 % of 0.35) to analyze the influence of f_{BC} on the $\mathrm{eBCMSD_{AAC-AE33}}$, as shown in Fig. 4c. $\mathrm{eBCMSD_{AAC-AE33}}$ was more influenced around 870 nm. The variation of f_{BC} led to uncertainty of ±3 % in $m_{\mathrm{eBC,bulk,AAC-AE33,200-720}}$, indicating that simplification of f_{BC} was a minor uncertainty source compared to MAC and transfer function inversion.

4.4 Uncertainty from instrumental noise

The instrumental noise stemmed from the fluctuation of the light source and flow of AE33, which was reflected as fluctuation in I, I_0 and F, further leading to the fluctuation in ATN, σ_{ATN} and σ_{ab}. The instrumental noise was defined as the SD of $\sigma_{\mathrm{ab,binned}}$ and is shown in Fig. S7b. It can be seen that the instrumental noise did not exhibit significant dependence on D_{p}. Comparing Fig. S7a and S7b, the instrumental noise was irrelevant to the value of $\sigma_{\mathrm{ab,binned}}$. Figure S7c illustrates that the instrumental noise was also not correlated to $\sigma_{\mathrm{ab,bulk}}$, with R^2, b_1 and b_0 of 0.0, 0.0 and 0.1 $\mathrm{M\,m^{-1}}$, respectively, implying that the instrumental noise was not dependent on the pollution level.

The SD of instrumental noise was added to (subtracted from) $\sigma_{\mathrm{ab,binned}}$, and the derived $\mathrm{eBCMSD_{AAC-AE33}}$ was used to study the influence of instrumental noise on $\mathrm{eBCMSD_{AAC-AE33}}$. The mean result is shown in Fig. 4d. $\mathrm{eBCMSD_{AAC-AE33}}$ larger than 1000 nm was more influenced by the instrumental noise than $\mathrm{eBCMSD_{AAC-AE33}}$ smaller than 500 nm. $\sigma_{\mathrm{ab,binned}}$ larger than 1000 nm was relatively small (about 0.3 $\mathrm{M\,m^{-1}}$) compared to $\sigma_{\mathrm{ab,binned}}$ less than 870 nm (about 0.9 $\mathrm{M\,m^{-1}}$). The mean instrumental noise was 0.1 $\mathrm{M\,m^{-1}}$ and exhibited no significant dependence on D_{p}. Therefore, $\sigma_{\mathrm{ab,binned}}$ larger than 1000 nm was more affected by the instrumental noise, resulting in distinct variation in $\mathrm{eBCMSD_{AAC-AE33}}$. The uncertainty in $m_{\mathrm{eBC,bulk,AAC-AE33,200-720}}$ was not obvious, which varied from −2 % to −1 %, also minor compared to MAC and transfer function inversion.

5 Summary

Knowledge of bulk black carbon (BC) characteristics, such as bulk BC mass concentration ($m_{\mathrm{BC,bulk}}$), is not sufficient for deeper understanding of the influence of BC on radiation and health. BC mass size distribution (BCMSD) was one of the BC microphysical characteristics that could indicate the emission source, reflect atmospheric aging and effectively reduce uncertainty related to BC radiative effect. However, current BCMSD measurement, ranging from upper submicron particle sizes to larger than 1 µm, was insufficient in time resolution and sophisticated for routine measurement. In this study, a new method to determine eBCMSD was proposed characterized by a wide size range of measurement up to 1.5 µm, a high time resolution up to 1 h and convenience for extensive measurement. The eBCMSD was retrieved by the size-resolved absorption coefficient ($\sigma_{\mathrm{ab,size\text{-}resolved}}$) measured by an aerodynamic aerosol classifier in tandem with an aethalometer model AE33 (AAC–AE33), denoted as $\mathrm{eBCMSD_{AAC-AE33}}$. Size-resolved number concentration ($N_{\mathrm{size\text{-}resolved}}$) was measured concurrently by a scanning mobility particle sizer (SMPS) and an aerodynamic particle sizer (APS) to model the influence of size on mass absorption cross-section (MAC). Uncertainty analysis was performed with respect to MAC, transfer function inversion, number fraction of BC-containing particle (f_{BC}) and instrumental noise, which led to 24 %, 11 %, 3 % and 0.5 % variation on the derived $m_{\mathrm{BC,bulk}}$, respectively.

The proposed method was applied to a field measurement in the Yangtze River Delta and validated by comparing the rBCMSD with that measured by a differential mobility analyzer in tandem with a single-particle soot photometer (DMA–SP2), denoted as $\mathrm{rBCMSD_{DMA-SP2}}$. The results showed that for a particle diameter (D_{p}) less than 300 nm, $\mathrm{eBCMSD_{AAC-AE33}}$ was higher than $\mathrm{rBCMSD_{DMA-SP2}}$, which might be caused by underestimated MAC using the method proposed by W. Zhao et al. (2021) or incomplete parameterization of spectral broadening of the AAC. $\mathrm{eBCMSD_{AAC-AE33}}$ was consistent with $\mathrm{rBCMSD_{DMA-SP2}}$ for D_{p} larger than 300 nm. $m_{\mathrm{BC,bulk}}$ integrated over the size range that AAC–AE33 and DMA–SP2 both measured (200–720 nm), denoted as $m_{\mathrm{eBC,bulk,AAC-AE33,200-720}}$ and $m_{\mathrm{rBC,bulk,DMA-SP2,200-720}}$, compared well with each other, with a determination coefficient (R^2), slope (b_1) and intercept (b_0) of 0.8, 1.0 and 0.1 $\mathrm{\mu g\,m^{-3}}$, respectively. However, the DMA–SP2 did not measure D_{p} values larger than 700 nm, leading to 0.2 $\mathrm{\mu g\,m^{-3}}$ (33 %) underestimation

of $m_{BC,bulk}$, highlighting the necessity to measure BCMSD with a wider size range.

As mentioned above, MAC was the largest uncertainty source, leading to significant uncertainty for D_p less than 300 nm. Transfer function inversion was the second largest uncertainty source, which was induced by incomplete parameterization of spectral broadening. The uncertainty in the transfer function inversion led to systematic overestimation of $m_{eBC,bulk,AAC-AE33,200-720}$, which was corrected in this study. Both f_{BC} and instrumental noise were minor uncertainty sources and 1 order of magnitude less than MAC and transfer function inversion. f_{BC} was a simplification of complicated BC mixing states, leading to relatively big uncertainty in eBCMSD at 870 nm, around the boundary between the condensation mode and droplet mode. The eBCMSD for D_p larger than 1000 nm was more sensitive to instrumental noise.

Code and data availability. The code and measurement data involved in this study are available upon request to the authors.

Supplement. The supplement related to this article is available online at: https://doi.org/10.5194/amt-15-6807-2022-supplement.

Author contributions. CZ determined the main goal of this study. WZ and GZ designed the methods. WZ carried experiments out and prepared the paper with contributions from all co-authors.

Competing interests. The contact author has declared that none of the authors has any competing interests.

Disclaimer. Publisher's note: Copernicus Publications remains neutral with regard to jurisdictional claims in published maps and institutional affiliations.

Financial support. This research has been supported by the National Natural Science Foundation of China (grant no. 41961160728).

Review statement. This paper was edited by Paolo Laj and reviewed by two anonymous referees.

References

Bond, T. C.: Spectral dependence of visible light absorption by carbonaceous particles emitted from coal combustion, Geophys. Res. Lett., 28, 4075–4078, https://doi.org/10.1029/2001GL013652, 2001.

Bond, T. C. and Bergstrom, R. W.: Light absorption by carbonaceous particles: An investigative review, Aerosol Sci. Tech., 40, 27–67, https://doi.org/10.1080/02786820500421521, 2006.

Bond, T. C., Streets, D. G., Yarber, K. F., Nelson, S. M., Woo, J. H., and Klimont, Z.: A technology-based global inventory of black and organic carbon emissions from combustion, J. Geophys. Res.-Atmos., 109, D14203, https://doi.org/10.1029/2003jd003697, 2004.

Bond, T. C., Doherty, S. J., Fahey, D. W., Forster, P. M., Berntsen, T., DeAngelo, B. J., Flanner, M. G., Ghan, S., Karcher, B., Koch, D., Kinne, S., Kondo, Y., Quinn, P. K., Sarofim, M. C., Schultz, M. G., Schulz, M., Venkataraman, C., Zhang, H., Zhang, S., Bellouin, N., Guttikunda, S. K., Hopke, P. K., Jacobson, M. Z., Kaiser, J. W., Klimont, Z., Lohmann, U., Schwarz, J. P., Shindell, D., Storelvmo, T., Warren, S. G., and Zender, C. S.: Bounding the role of black carbon in the climate system: A scientific assessment, J. Geophys. Res.-Atmos., 118, 5380–5552, https://doi.org/10.1002/jgrd.50171, 2013.

Castagna, J., Calvello, M., Esposito, F., and Pavese, G.: Analysis of equivalent black carbon multi-year data at an oil pre-treatment plant: Integration with satellite data to identify black carbon transboundary sources, Remote Sens. Environ., 235, 111429, https://doi.org/10.1016/j.rse.2019.111429, 2019.

Chow, J. C., Watson, J. G., Crow, D., Lowenthal, D. H., and Merrifield, T.: Comparison of IMPROVE and NIOSH Carbon Measurements, Aerosol Sci. Tech., 34, 23–34, https://doi.org/10.1080/02786820119073, 2001.

DeCarlo, P. F., Slowik, J. G., Worsnop, D. R., Davidovits, P., and Jimenez, J. L.: Particle Morphology and Density Characterization by Combined Mobility and Aerodynamic Diameter Measurements. Part 1: Theory, Aerosol Sci. Tech., 38, 1185–1205, https://doi.org/10.1080/027868290903907, 2004.

Drinovec, L., Močnik, G., Zotter, P., Prévôt, A. S. H., Ruckstuhl, C., Coz, E., Rupakheti, M., Sciare, J., Müller, T., Wiedensohler, A., and Hansen, A. D. A.: The "dual-spot" Aethalometer: an improved measurement of aerosol black carbon with real-time loading compensation, Atmos. Meas. Tech., 8, 1965–1979, https://doi.org/10.5194/amt-8-1965-2015, 2015.

Guo, Y. H.: Carbonaceous aerosol composition over northern China in spring 2012, Environ. Sci. Pollut. Res., 22, 10839–10849, https://doi.org/10.1007/s11356-015-4299-8, 2015.

Hansen, A. D. A., Rosen, H., and Novakov, T.: The aethalometer - an instrument for the real-time measurement of optical-absorption by aerosol-particles, Sci. Total Environ., 36, 191–196, https://doi.org/10.1016/0048-9697(84)90265-1, 1984.

Helin, A., Niemi, J. V., Virkkula, A., Pirjola, L., Teinila, K., Backman, J., Aurela, M., Saarikoski, S., Ronkko, T., Asmi, E., and Timonen, H.: Characteristics and source apportionment of black carbon in the Helsinki metropolitan area, Finland, Atmos. Environ., 190, 87–98, https://doi.org/10.1016/j.atmosenv.2018.07.022, 2018.

Highwood, E. J. and Kinnersley, R. P.: When smoke gets in our eyes: The multiple impacts of atmospheric black carbon on climate, air quality and health, Environ. Int., 32, 560–566, https://doi.org/10.1016/j.envint.2005.12.003, 2006.

Johnson, T. J., Irwin, M., Symonds, J. P. R., Olfert, J. S., and Boies, A. M.: Measuring aerosol size distributions with the aerodynamic aerosol classifier, Aerosol Sci. Tech., 52, 655–665, https://doi.org/10.1080/02786826.2018.1440063, 2018.

Karlsson, M. N. A. and Martinsson, B. G.: Methods to measure and predict the transfer function size dependence of individual DMAs, J. Aerosol Sci., 34, 603–625, https://doi.org/10.1016/s0021-8502(03)00020-x, 2003.

Kim, J. H., Mulholland, G. W., Kukuck, S. R., and Pui, D. Y. H.: Slip correction measurements of certified PSL nanoparticles using a nanometer differential mobility analyzer (nano-DMA) for Knudsen number from 0.5 to 83, J. Res. Natl. Inst. Stan., 110, 31–54, https://doi.org/10.6028/jres.110.005, 2005.

Knutson, E. O. and Whitby, K. T.: Aerosol classification by electric mobility: apparatus, theory, and applications, J. Aerosol Sci., 6, 443–451, https://doi.org/10.1016/0021-8502(75)90060-9, 1975.

Liu, C., Chung, C. E., Yin, Y., and Schnaiter, M.: The absorption Ångström exponent of black carbon: from numerical aspects, Atmos. Chem. Phys., 18, 6259–6273, https://doi.org/10.5194/acp-18-6259-2018, 2018.

Liu, D., Flynn, M., Gysel, M., Targino, A., Crawford, I., Bower, K., Choularton, T., Jurányi, Z., Steinbacher, M., Hüglin, C., Curtius, J., Kampus, M., Petzold, A., Weingartner, E., Baltensperger, U., and Coe, H.: Single particle characterization of black carbon aerosols at a tropospheric alpine site in Switzerland, Atmos. Chem. Phys., 10, 7389–7407, https://doi.org/10.5194/acp-10-7389-2010, 2010.

Matsui, H., Hamilton, D. S., and Mahowald, N. M.: Black carbon radiative effects highly sensitive to emitted particle size when resolving mixing-state diversity, Nat. Commun., 9, 3446, https://doi.org/10.1038/s41467-018-05635-1, 2018.

Moosmuller, H., Chakrabarty, R. K., and Arnott, W. P.: Aerosol light absorption and its measurement: A review, J. Quant. Spectrosc. Ra., 110, 844–878, https://doi.org/10.1016/j.jqsrt.2009.02.035, 2009.

Ning, Z., Chan, K. L., Wong, K. C., Westerdahl, D., Mocnik, G., Zhou, J. H., and Cheung, C. S.: Black carbon mass size distributions of diesel exhaust and urban aerosols measured using differential mobility analyzer in tandem with Aethalometer, Atmos. Environ., 80, 31–40, https://doi.org/10.1016/j.atmosenv.2013.07.037, 2013.

Onasch, T. B., Trimborn, A., Fortner, E. C., Jayne, J. T., Kok, G. L., Williams, L. R., Davidovits, P., and Worsnop, D. R.: Soot Particle Aerosol Mass Spectrometer: Development, Validation, and Initial Application, Aerosol Sci. Tech., 46, 804–817, https://doi.org/10.1080/02786826.2012.663948, 2012.

Petzold, A., Ogren, J. A., Fiebig, M., Laj, P., Li, S.-M., Baltensperger, U., Holzer-Popp, T., Kinne, S., Pappalardo, G., Sugimoto, N., Wehrli, C., Wiedensohler, A., and Zhang, X.-Y.: Recommendations for reporting "black carbon" measurements, Atmos. Chem. Phys., 13, 8365–8379, https://doi.org/10.5194/acp-13-8365-2013, 2013.

Ramachandran, S. and Rajesh, T. A.: Black carbon aerosol mass concentrations over Ahmedabad, an urban location in western India: Comparison with urban sites in Asia, Europe, Canada, and the United States, J. Geophys. Res.-Atmos., 112, D06211, https://doi.org/10.1029/2006jd007488, 2007.

Ran, L., Deng, Z. Z., Wang, P. C., and Xia, X. A.: Black carbon and wavelength-dependent aerosol absorption in the North China Plain based on two-year aethalometer measurements, Atmos. Environ., 142, 132–144, https://doi.org/10.1016/j.atmosenv.2016.07.014, 2016.

Schwarz, J. P., Gao, R. S., Fahey, D. W., Thomson, D. S., Watts, L. A., Wilson, J. C., Reeves, J. M., Darbeheshti, M., Baumgardner, D. G., Kok, G. L., Chung, S. H., Schulz, M., Hendricks, J., Lauer, A., Karcher, B., Slowik, J. G., Rosenlof, K. H., Thompson, T. L., Langford, A. O., Loewenstein, M., and Aikin, K. C.: Single-particle measurements of midlatitude black carbon and light-scattering aerosols from the boundary layer to the lower stratosphere, J. Geophys. Res.-Atmos., 111, D16207, https://doi.org/10.1029/2006jd007076, 2006.

Schwarz, J. P., Spackman, J. R., Fahey, D. W., Gao, R. S., Lohmann, U., Stier, P., Watts, L. A., Thomson, D. S., Lack, D. A., Pfister, L., Mahoney, M. J., Baumgardner, D., Wilson, J. C., and Reeves, J. M.: Coatings and their enhancement of black carbon light absorption in the tropical atmosphere, J. Geophys. Res.-Atmos., 113, D03203, https://doi.org/10.1029/2007jd009042, 2008.

Soto-García, L. L., Andreae, M. O., Andreae, T. W., Artaxo, P., Maenhaut, W., Kirchstetter, T., Novakov, T., Chow, J. C., and Mayol-Bracero, O. L.: Evaluation of the carbon content of aerosols from the burning of biomass in the Brazilian Amazon using thermal, optical and thermal-optical analysis methods, Atmos. Chem. Phys., 11, 4425–4444, https://doi.org/10.5194/acp-11-4425-2011, 2011.

Tavakoli, F. and Olfert, J. S.: An Instrument for the Classification of Aerosols by Particle Relaxation Time: Theoretical Models of the Aerodynamic Aerosol Classifier, Aerosol Sci. Tech., 47, 916–926, https://doi.org/10.1080/02786826.2013.802761, 2013.

Taylor, J. W., Allan, J. D., Liu, D., Flynn, M., Weber, R., Zhang, X., Lefer, B. L., Grossberg, N., Flynn, J., and Coe, H.: Assessment of the sensitivity of core / shell parameters derived using the single-particle soot photometer to density and refractive index, Atmos. Meas. Tech., 8, 1701–1718, https://doi.org/10.5194/amt-8-1701-2015, 2015.

Tunved, P., Cremer, R. S., Zieger, P., and Strom, J.: Using correlations between observed equivalent black carbon and aerosol size distribution to derive size resolved BC mass concentration: a method applied on long-term observations performed at Zeppelin station, Ny-Ålesund, Svalbard, Tellus B, 73, 1–17, https://doi.org/10.1080/16000889.2021.1933775, 2021.

Viidanoja, J., Kerminen, V.-M., and Hillamo, R.: Measuring the Size Distribution of Atmospheric Organic and Black Carbon Using Impactor Sampling Coupled with Thermal Carbon Analysis: Method Development and Uncertainties, Aerosol Sci. Tech., 36, 607–616, https://doi.org/10.1080/02786820252883847, 2002.

Wang, J. D., Wang, S. X., Wang, J. P., Hua, Y., Liu, C., Cai, J., Xu, Q. C., Xu, X. T., Jiang, S. Y., Zheng, G. J., Jiang, J. K., Cai, R. L., Zhou, W., Chen, G. Z., Jin, Y. Z., Zhang, Q., and Hao, J. M.: Significant Contribution of Coarse Black Carbon Particles to Light Absorption in North China Plain, Environ. Sci. Tech. Let., 9, 134–139, https://doi.org/10.1021/acs.estlett.1c00953, 2022.

Yu, H., Wu, C., Wu, D., and Yu, J. Z.: Size distributions of elemental carbon and its contribution to light extinction in urban and rural locations in the pearl river delta region, China, Atmos. Chem. Phys., 10, 5107–5119, https://doi.org/10.5194/acp-10-5107-2010, 2010.

Zhang, R. Y., Khalizov, A. F., Pagels, J., Zhang, D., Xue, H. X., and McMurry, P. H.: Variability in morphology, hygroscopicity, and optical properties of soot aerosols during atmospheric processing, P. Natl. Acad. Sci. USA, 105, 10291–10296, https://doi.org/10.1073/pnas.0804860105, 2008.

Zhao, G., Tao, J., Kuang, Y., Shen, C., Yu, Y., and Zhao, C.: Role of black carbon mass size distribution in the direct aerosol radiative forcing, Atmos. Chem. Phys., 19, 13175–13188, https://doi.org/10.5194/acp-19-13175-2019, 2019.

Zhao, G., Shen, C. Y., and Zhao, C. S.: Technical note: Mismeasurement of the core-shell structure of black carbon-containing ambient aerosols by SP2 measurements, Atmos. Environ., 243, 117885, https://doi.org/10.1016/j.atmosenv.2020.117885, 2020a.

Zhao, G., Yu, Y., Tian, P., Li, J., Guo, S., and Zhao, C.: Evaluation and Correction of the Ambient Particle Spectral Light Absorption Measured Using a Filter-based Aethalometer, Aerosol Air Qual. Res., 20, 1833–1841, https://doi.org/10.4209/aaqr.2019.10.0500, 2020b.

Zhao, G., Tan, T., Zhu, Y., Hu, M., and Zhao, C.: Method to quantify black carbon aerosol light absorption enhancement with a mixing state index, Atmos. Chem. Phys., 21, 18055–18063, https://doi.org/10.5194/acp-21-18055-2021, 2021.

Zhao, W., Tan, W., Zhao, G., Shen, C., Yu, Y., and Zhao, C.: Determination of equivalent black carbon mass concentration from aerosol light absorption using variable mass absorption cross section, Atmos. Meas. Tech., 14, 1319–1331, https://doi.org/10.5194/amt-14-1319-2021, 2021.